

# Stability of intrinsic defects and defect clusters in $\text{LiNbO}_3$ from density functional theory calculations

Haixuan Xu (徐海讚),<sup>1</sup> Donghwa Lee (이동화),<sup>1</sup> Jun He (贺峻),<sup>1,\*</sup> Susan B. Sinnott,<sup>1</sup> Venkatraman Gopalan,<sup>2</sup> Volkmar Dierolf,<sup>3</sup> and Simon R. Phillpot<sup>1,†</sup>

<sup>1</sup>*Department of Materials Science and Engineering, University of Florida, Gainesville, Florida 32611, USA*

<sup>2</sup>*Department of Materials Science and Engineering, Pennsylvania State University, University Park, Pennsylvania 16802, USA*

<sup>3</sup>*Department of Physics, Lehigh University, Bethlehem, Pennsylvania 18015, USA*

(Received 19 May 2008; revised manuscript received 22 September 2008; published 6 November 2008)

A large experimental body of literature on lithium niobate, a technologically important ferroelectric, suggests that nonstoichiometric defects dominate its physical behavior, from macroscale switching to nanoscale wall structure. The exact structure and energetics of such proposed intrinsic defects and defect clusters remains unverified by either first-principles calculations or experiments. Here, density functional theory (DFT) is used to determine the dominant intrinsic defects in  $\text{LiNbO}_3$  under various conditions. In particular, in an  $\text{Nb}_2\text{O}_5$ -rich environment, a cluster consisting of a niobium antisite compensated by four lithium vacancies is predicted to be the most stable defect structure, thereby verifying what was thus far a conjecture in the literature. Under  $\text{Li}_2\text{O}$ -rich conditions, the lithium Frenkel defect is predicted to be the most stable, with a positive defect formation energy (DFE). This is proposed as the underlying reason that the vapor-transport equilibration (VTE) method can grow stoichiometric  $\text{LiNbO}_3$ . The effects of temperature and oxygen partial pressure are also explored by combining the DFT results with thermodynamic calculations. These predictions provide a picture of a very rich defect structure in lithium niobate, which has important effects on its physical behavior at the macroscale.

DOI: [10.1103/PhysRevB.78.174103](https://doi.org/10.1103/PhysRevB.78.174103)

PACS number(s): 61.72.J-, 71.15.Mb, 61.82.Ms

## I. INTRODUCTION

$\text{LiNbO}_3$  is an important ferro-, pyro-, and piezoelectric material with many promising physical properties.<sup>1</sup> Its applications include use as a second-harmonic generator, a parametric oscillator, a transducer, and nonvolatile memory.<sup>2,3</sup> Nonstoichiometric intrinsic defects and defect clusters have been identified as the origin of substantial differences in properties between materials with slightly different Li/Nb ratios. While a large body of experimental literature exists, and some theoretical investigations have been performed, many of the key conjectures in the literature, especially on defect clusters, remain unverified by either experiments or theory. The purpose of this work is to systematically analyze the intrinsic defects and defect clusters in lithium niobate using density functional theory (DFT) calculations combined with thermodynamic calculations.

It appears that the growth process affects the type of defects produced. The typical composition of  $\text{LiNbO}_3$  grown from congruent melting is  $\text{Li}/(\text{Li}+\text{Nb})=0.485$ , which indicates a lithium-deficient defect structure.<sup>4</sup> More nearly stoichiometric compositions have been achieved through vapor-transport equilibration (VTE) (Refs. 5 and 6) and double-crucible Czochralski (DCCZ) (Refs. 7 and 8) methods. The change in composition from 0.485 (congruent) to 0.5 (stoichiometric) causes large shifts in the Curie temperature,<sup>9</sup> cohesive field for domain reversal,<sup>8-10</sup> built-in internal field,<sup>11</sup> and other properties.<sup>4</sup> In particular, it has been conjectured that the temperature stability and field dynamics of a defect cluster consisting of a niobium antisite surrounded by four lithium vacancies can explain much of the observed macroscale switching behavior in congruent lithium niobate.<sup>4</sup> However, no experimental verification or detailed theoretical

analysis of this intrinsic defect cluster has been presented to date. Thus, a fundamental understanding of this and other intrinsic defects in  $\text{LiNbO}_3$  is essential.

Based on the experimental data, several defect models in congruent  $\text{LiNbO}_3$  have been proposed. Prokhorov and Kuzminov<sup>12</sup> proposed that oxygen vacancies surrounded by two lithium vacancies (the so-called model I) dominate at room temperature. However, it was soon determined from experiments that the density of  $\text{LiNbO}_3$  increases with increasing  $\text{Li}_2\text{O}$  deficiency,<sup>13</sup> which is inconsistent with model I. Schirmer *et al.*<sup>14</sup> concluded that niobium antisites compensated by niobium vacancies (model II) are the dominant defects, and that oxygen vacancies are present in negligible concentration. However, Donnerberg *et al.*,<sup>15</sup> using atomic-level simulations, showed that the formation of niobium vacancies to compensate for the niobium antisites is energetically less favorable than the formation of lithium vacancies. This leads to model III consisting of  $\text{Nb}_{\text{Li}}^{\cdots} + 4V_{\text{Li}}'$  (Fig. 1). Model III was supported by x-ray- and neutron-diffraction studies.<sup>16-19</sup> On the one hand, Schirmer *et al.*<sup>14</sup> pointed out that the niobium vacancy model (model II) and lithium vacancy model (model III) can be reconciled if it is assumed that there are ilmenite-type stacking faults in congruent  $\text{LiNbO}_3$ . On the other hand, nuclear-magnetic-resonance (NMR) studies<sup>20,21</sup> concluded that a combination of model I and model III provides both qualitative and quantitative agreement with Li NMR spectra. Inconsistent with this is the assumption that only model III can be used to explain the temperature dependence of experimental Li and Nb NMR spectra.<sup>20,21</sup> These contradictory experimental results demonstrate that the nature of intrinsic-defect arrangements in  $\text{LiNbO}_3$  is still not fully understood.

In order to understand intrinsic-defect complexes, it is first necessary to understand the formation of individual

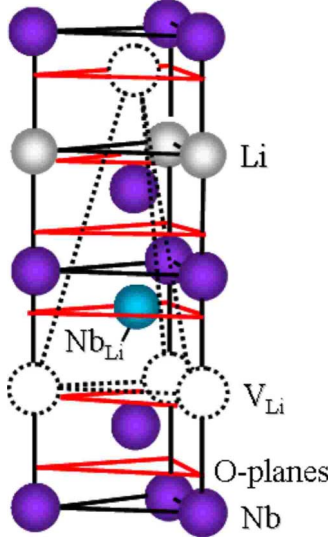


FIG. 1. (Color online) Schematic of possible defect arrangement involving one  $\text{Nb}_{\text{Li}}$  and four  $\text{V}_{\text{Li}}$  (so-called model III).

point defects. First-principles calculations have played a critical role in characterizing the interplay of defects and impurities on physical properties in many materials.<sup>22–24</sup> Here, DFT is employed to make quantitative predictions of the stability of various intrinsic point defects and defect clusters in  $\text{LiNbO}_3$ . In particular, the defect formation energies (DFEs) of intrinsic point defects and defect clusters under various conditions are calculated and the dominant defects, which have the lowest DFEs, are determined. Furthermore, the local structures of stable defects are determined. The effects of temperature and oxygen partial pressure on DFEs are also predicted through the combination of the DFT results with thermodynamic calculations. These investigations also allow us to speculate on the origins of the experimentally found dependence of defect chemistry on the sample history (e.g., annealing<sup>25</sup>).

Defect energetics in  $\text{LiNbO}_3$  was investigated long ago by Donnerberg *et al.*<sup>26</sup> using empirical potentials. However, it is known that electronic-structure methods are usually more accurate than empirical approaches. Moreover, at that time the thermodynamics framework required to analyze nonstoichiometric defects had not been established. Indeed, the combination of electronic-structure calculations and thermodynamic analysis used here will enable a comprehensive and quantitative analysis of the intrinsic-defect chemistry. Some of the questions addressed here have also been addressed in a recent analysis, also using DFT.<sup>27</sup> Unfortunately, a number of the key results seem to be physically unreasonable. For example, the calculated formation energy of a  $\text{V}_{\text{Nb}}$  was determined to be  $-114.46$  and  $+13.49$  eV depending on whether the supercell considered contains 80 atoms or 180 atoms. It thus appears worthwhile to re-examine the energetics of point defects in  $\text{LiNbO}_3$ .

## II. METHODOLOGY

The Vienna *Ab Initio* Simulation Package (VASP) (Refs. 28 and 29) is employed to carry out all the calculations of crys-

TABLE I. Lattice parameters calculated by PAW-LDA and PAW-GGA, compared with previous results. USPP denotes ultrasoft pseudopotential; NCPP denotes norm-conserving pseudopotential.

	$a$ (Å)	$c$ (Å)	$V$ (Å <sup>3</sup> )
PAW-LDA	5.049	13.686	302.198
PAW-GGA	5.138	13.914	318.119
USPP-LDA <sup>a</sup>	5.064	13.667	303.523
USPP-LDA <sup>b</sup>	5.086	13.723	307.420
NCPP-LDA <sup>c</sup>	5.125	13.548	308.172
NCPP-GGA <sup>c</sup>	5.255	13.791	329.816
Exp.	5.147 <sup>d</sup>	13.853 <sup>d</sup>	317.873 <sup>d</sup>
	5.151 <sup>e</sup>	13.876 <sup>e</sup>	318.844 <sup>e</sup>

<sup>a</sup>Reference 27.

<sup>b</sup>Reference 35.

<sup>c</sup>Reference 34.

<sup>d</sup>Reference 61.

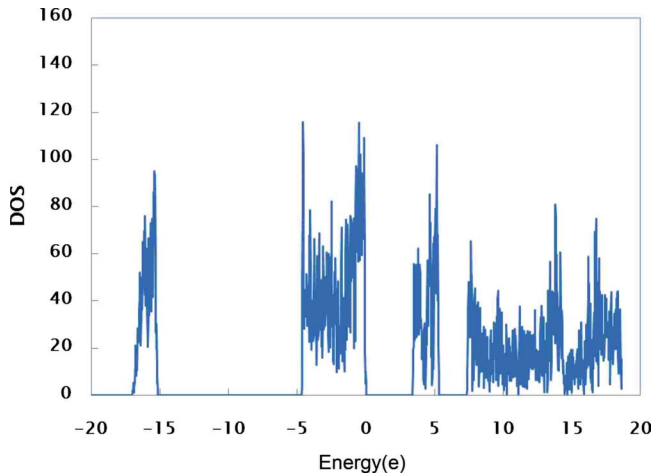
<sup>e</sup>Reference 62.

tallographic structures, electronic structures, and defect formation energies. The projected augmented wave (PAW) method,<sup>30</sup> which combines much of the accuracy of an all-electron method<sup>31</sup> with the flexibility of the pseudo-potential approach,<sup>32</sup> is used. The Li  $2s^1$ , Nb  $4p^64d^45s^1$ , and O  $2s^22p^4$  are treated as valence electrons. The cutoff energy for plane-wave basis set is 400 eV.<sup>27</sup> The allowed error in energy from relaxation is 0.001 eV. The electronic minimization algorithm for energy calculation is based on residual minimization scheme-direct inversion in the iterative subspace (RMM-DIIS).<sup>33</sup>

### A. LDA versus GGA

The results obtained from the local-density approximation (LDA) and the general gradient approximation (GGA) for the lattice parameters of the ferroelectric phase of  $\text{LiNbO}_3$  ( $R3c$ ) are compared with experimental values in Table I for a supercell containing  $2 \times 2 \times 2$  conventional unit cells (240 atoms with a total of 1440 electrons). As is typical, GGA predicts larger lattice parameters than LDA. As Table I shows, GGA gives excellent agreement with the experimental values, with the in-plane lattice parameter  $a$  being underestimated by 0.2% and the  $c$  lattice parameter being overestimated by 0.6%. As a result the calculated volume is within 0.1% of the experimental value. The GGA-PAW calculations give considerably better agreement with experimental values than the LDA and GGA calculations with the norm-conserving pseudopotentials (NCPPs) (Ref. 34) or LDA calculations with ultrasoft pseudopotentials (USPPs).<sup>27,35</sup>

The electronic densities of states (DOSs) have been calculated using PAW-LDA and PAW-GGA. LDA yields a band gap of 3.42 eV, whereas the GGA value is 3.5 eV. These results are consistent with previous calculations using NCPPs of 3.48 and 3.50 eV for LDA and GGA, respectively.<sup>34</sup> This calculated band gap is also in good agreement with the value of 3.5 eV, previously calculated

FIG. 2. (Color online) The DOS for  $\text{LiNbO}_3$ .

using the orthogonalized-linear-combination-of-atomic-orbital (OLCAO) method.<sup>36</sup> The band gap calculated by GGA is 8% less than the experimental value of 3.78 eV.<sup>37,38</sup> This agreement can be considered as excellent, since DFT is widely known to underestimate band gaps.<sup>39</sup> The DOS calculated using GGA is given in Fig. 2. The highest occupied valence band exhibits mainly O  $2p$  features, whereas the lowest unoccupied conduction band mainly consists of Nb  $4d$  electrons. This DOS is also consistent with calculations performed by OLCAO (Ref. 36) and NCPP.<sup>34</sup> Based on this analysis of structure and band structure, GGA is chosen for the calculations of DFEs.

### B. $k$ -point mesh

The Monkhorst-Pack<sup>40</sup> method is used to carry out the integration in the Brillouin zone. Since for  $\text{LiNbO}_3$ , the length of  $c$  is approximately double that of  $a$  for a  $2 \times 2 \times 2$  system, we chose to have half the number of  $k$  points in the  $z$  direction ( $c$  axis) as in the  $x$  and  $y$  directions. A  $4 \times 4 \times 2$   $k$ -point mesh has been used in the current study for both the perfect-structure and defect-structure calculations. As discussed by Van de Walle and Neugebauer,<sup>22</sup> the  $\Gamma$  point should be avoided for an accurate calculation of the DFEs because the interaction between a defect and its mirror image through periodic boundary conditions is at its maximum at the  $\Gamma$  point. Thus, the origin of the  $k$ -point mesh has been shifted from the  $\Gamma$  point to  $(0.5, 0.5, 0.5)$ .

### C. System size

The supercell method,<sup>41–43</sup> containing a finite number of atoms and defects with periodic boundary conditions, is used to calculate the formation energies of both isolated defects and defect clusters. In general, the larger the supercell is, the smaller is the error due to the interaction between the defect and its mirror image, thereby more closely approximating the dilute limit that we wish to capture. Because larger supercells require a formidable amount of computational time, we have systematically analyzed the system-size convergence. To characterize the convergence, supercell sizes of  $1 \times 1 \times 1$ ,

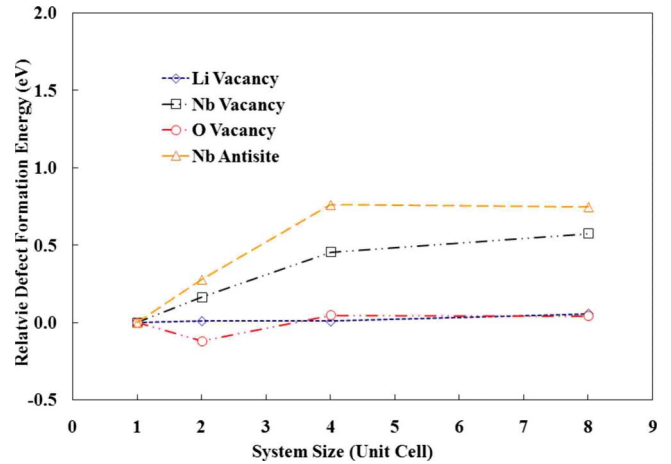


FIG. 3. (Color online) Difference in defect formation energy (relative to the  $1 \times 1 \times 1$  system) as a function of system size. Supercell sizes of  $1 \times 1 \times 1$ ,  $2 \times 1 \times 1$ ,  $2 \times 2 \times 1$ , and  $2 \times 2 \times 2$  correspond to 1, 2, 4, and 8 in the  $x$  axis.

$2 \times 1 \times 1$ ,  $2 \times 2 \times 1$ , and  $2 \times 2 \times 2$ , containing 30, 60, 120, and 240 atoms, respectively, are considered. The difference in DFE as a function of supercell size is calculated; the results of typical cases are shown in Fig. 3. As Fig. 3 shows, the 120-atom supercell and 240-atom supercell produce similar results for various types of vacancies and niobium antisites (see also Table II). The larger size effects for the Nb vacancy and Nb antisite are presumably due to their larger charges and point to the dominant effects of electrostatic charge on artificial defect-defect interactions. Based on the energies of the two larger system sizes, the error on DFE from supercell-size effects is estimated to be  $\sim 0.1$ – $0.2$  eV.

For the neutral defect clusters, the electrostatic contribution to the system-size dependence can be expected to be rather small and only due to dipole and higher multipole interactions. However, the strain contribution can be expected to be larger than for the point defects considered in Fig. 3. As discussed below, from the analysis of the energy differences between defect reactions, the size dependence is expected to be weak enough that we can be confident in the conclusions drawn. Therefore, all of the analyses reported are based on results obtained from the  $2 \times 2 \times 2$  (240-atom) supercell.

Even for the relatively large system used here, the precise optimization method can have an effect on the results obtained. The approach used here follows the scheme of Van de Walle and Neugebauer.<sup>22</sup> In particular, the defects are added to an optimized perfect-crystal structure and then the positions of all atoms within  $4.5 \text{ \AA}$  of the defect are optimized.<sup>22</sup> This implies that within a system of 240 atoms approximately 116 atoms are relaxed for all the defect cases. The

TABLE II. Differences in DFE between  $2 \times 2 \times 1$  system and  $2 \times 2 \times 2$  system for various defects.

	Li vacancy	O vacancy	Nb vacancy	Nb antisite
Difference (eV)	0.051	-0.005	0.121	-0.014

DFE calculated in this manner differs from that obtained from a full optimization of all the atomic positions by 0.052, 0.050, and 0.140 eV for the Li vacancy, O vacancy, and Nb antisite, respectively. A similar approximation has been used for defects in GaN (Ref. 22) and ZnO systems.<sup>23</sup>

An alternative to using large system sizes to minimize the effects of the artificial interactions between defects and their images would be to compensate for them in an analytic manner. In particular, Makov and Payne<sup>44</sup> developed a general approach to correct the calculation for cubic system. However, this approach has been found to lead to an overestimate of the correction term for some semiconductor systems.<sup>22,45,46</sup> We have not included a Makov-Payne correction in our charged supercell analysis, but rather rely on our system size being sufficiently large, an assumption that we justify by the data in Fig. 3.

### III. THERMODYNAMIC FRAMEWORK

#### A. Defect formation energy

The DFE of a defect or defects, denoted as  $\alpha$ , with charge state  $q$  is defined as<sup>22</sup>

$$\Delta E_f(\alpha, q, T, P) = E^{\text{total}}(\alpha, q) - E^{\text{total}}(\text{perfect}) + \sum_i n_i \mu_i - q(\varepsilon_F + E_v + \Delta V), \quad (1)$$

where  $E^{\text{total}}(\alpha, q)$  is the total energy obtained from DFT calculation of a supercell with the defect(s).  $E^{\text{total}}(\text{perfect})$  is the total energy of the supercell without any defects.  $n_i$  is the number of atoms of species  $i$  that have been added to ( $n_i > 0$ ) or removed from ( $n_i < 0$ ) the supercell when the defects are created.  $\mu_i$  is the chemical potential of element  $i$ .  $T$  is temperature and  $P$  is the oxygen partial pressure.  $\varepsilon_F$  is the Fermi energy with respect to the valence-band maximum (VBM) in the bulk single crystal.  $E_v$  is the VBM of the bulk single-crystal system. Therefore, as discussed by Van de Walle and Neugebauer,<sup>22</sup> a correction term  $\Delta V$ , which is the difference between the electrostatic potentials of the defected and undefected systems, is needed to align the band structures.

Strictly speaking, the free energy rather than the total energy should be used in Eq. (1) for the calculation of the DFEs. The total internal energies of a supercell obtained from DFT calculations correspond to the Helmholtz free energy at zero temperature, neglecting zero-point vibrations.<sup>47</sup> These calculations thus neglect the contributions from the vibrational entropy. Fortunately, experimental and theoretical results for entropies of point defects typically fall between 0 and  $10k$  (0–0.26 eV at 300 K), where  $k$  is the Boltzmann constant.<sup>22</sup> As a consequence, we do not expect this neglect of the entropy term to qualitatively change our conclusions. Detailed analyses by He *et al.*<sup>24</sup> and Kohan *et al.*<sup>23</sup> also concluded that entropic effects can be neglected.

#### B. Formalism for chemical potential in ternary oxides

As Eq. (1) shows, the formation energy of a defect or a defect cluster depends on the chemical potential of the ions

added or removed from the perfect crystal to form the defect. Below we outline a thermodynamically consistent process to determine the physically possible range of chemical potentials. This was first developed in the context of binary oxides.<sup>23,47</sup> The extension to ternary oxides used here is substantially the same as that used previously for LiNbO<sub>3</sub>,<sup>27</sup> BaTiO<sub>3</sub>,<sup>48</sup> and SrTiO<sub>3</sub>.<sup>49</sup>

The stability of the system against decomposition into its constituent elements places upper limits on the chemical potential of each element in LiNbO<sub>3</sub>,

$$\mu_{\text{Li}}[\text{LiNbO}_3] \leq \mu_{\text{Li}}[\text{metal}], \quad (2)$$

$$\mu_{\text{Nb}}[\text{LiNbO}_3] \leq \mu_{\text{Nb}}[\text{metal}], \quad (3)$$

$$\mu_{\text{O}}[\text{LiNbO}_3] \leq \mu_{\text{O}}[\text{O}_2]. \quad (4)$$

The total energy of a stoichiometric unit of LiNbO<sub>3</sub> can be expressed as

$$\mu_{\text{Li}}[\text{LiNbO}_3] + \mu_{\text{Nb}}[\text{LiNbO}_3] + 3\mu_{\text{O}}[\text{LiNbO}_3] = E_{\text{tot}}[\text{LiNbO}_3]. \quad (5)$$

Thus lower limits of chemical potential for each element can then be obtained,

$$\mu_{\text{O}}[\text{LiNbO}_3] \geq \frac{1}{3}(E_{\text{tot}}[\text{LiNbO}_3] - \mu_{\text{Li}}[\text{metal}] - \mu_{\text{Nb}}[\text{metal}]), \quad (6)$$

$$\mu_{\text{Li}}[\text{LiNbO}_3] \geq E_{\text{tot}}[\text{LiNbO}_3] - 3\mu_{\text{O}}[\text{O}_2] - \mu_{\text{Nb}}[\text{metal}], \quad (7)$$

$$\mu_{\text{Nb}}[\text{LiNbO}_3] \geq E_{\text{tot}}[\text{LiNbO}_3] - 3\mu_{\text{O}}[\text{O}_2] - \mu_{\text{Li}}[\text{metal}]. \quad (8)$$

Furthermore, since neither Li<sub>2</sub>O nor Nb<sub>2</sub>O<sub>5</sub> precipitates from bulk LiNbO<sub>3</sub>, the ranges of chemical potentials are subject to the additional constraints

$$2\mu_{\text{Li}}[\text{LiNbO}_3] + \mu_{\text{O}}[\text{LiNbO}_3] \leq E_{\text{tot}}[\text{Li}_2\text{O}], \quad (9)$$

$$2\mu_{\text{Nb}}[\text{LiNbO}_3] + 5\mu_{\text{O}}[\text{LiNbO}_3] \leq E_{\text{tot}}[\text{Nb}_2\text{O}_5]. \quad (10)$$

The above sets of equations define the ranges of chemical potential consistent with the stability of LiNbO<sub>3</sub> against decomposition into binary oxides or into its elemental components.

Knowing the boundary of chemical potential for each element, the range of possible values for the DFEs of single-point defects can be calculated. To fully characterize the defect reaction, knowledge of the range of chemical potentials is not sufficient: the chemical potential of each element has to be known.

Physically, it is possible to change the oxygen chemical potential through the temperature and/or oxygen partial pressure. There are two limits on the oxygen chemical potential in LiNbO<sub>3</sub>. Under extremely oxidizing conditions, the chemical potential of oxygen reaches its maximum. The criterion for the equilibrium of oxygen in LiNbO<sub>3</sub> and O<sub>2</sub> is

$$\mu_{\text{O}}[\text{LiNbO}_3] = \mu_{\text{O}}[\text{O}_2]. \quad (11)$$

Under reducing conditions, the Li and Nb in  $\text{LiNbO}_3$  must be in equilibrium with metallic Li and Nb. This places a lower limit on the oxygen chemical potential of

$$\mu_{\text{O}}[\text{LiNbO}_3] = \frac{1}{3}(E_{\text{tot}}[\text{LiNbO}_3] - \mu_{\text{Li}}[\text{metal}] - \mu_{\text{Nb}}[\text{metal}]). \quad (12)$$

As we shall see, these constraints actually correspond to unrealistically high and low oxygen partial pressures, with the physically attainable range of partial pressures being much narrower.

Bringing all of these stability criteria together, we can construct the ternary chemical-potential map shown in Fig. 4, where the points in chemical-potential space should be analyzed in a manner analogous to that for the composition in a conventional ternary phase diagram.<sup>50</sup> In the following, the points and lines refer to the ternary chemical potential map in Fig. 4.

### 1. Case A: $\text{Li}_2\text{O}$ reference state (line AD)

When  $\text{Li}_2\text{O}$  is chosen as a reference state, the composition-weighted sum of the lithium and oxygen chemical potentials is equal to the total energy of  $\text{Li}_2\text{O}$ . Likewise the criterion for the equilibrium of Li in  $\text{LiNbO}_3$  and  $\text{Li}_2\text{O}$  is

$$\mu_{\text{Li}}^{\text{Li}_2\text{O}}[\text{LiNbO}_3] = \frac{1}{2}(E_{\text{tot}}[\text{Li}_2\text{O}] - \mu_{\text{O}}). \quad (13)$$

The chemical potential of Nb in  $\text{LiNbO}_3$  can then be determined:

$$\mu_{\text{Nb}}^{\text{Li}_2\text{O}}[\text{LiNbO}_3] = E_{\text{tot}}[\text{LiNbO}_3] - 3\mu_{\text{O}} - \mu_{\text{Li}}^{\text{Li}_2\text{O}}[\text{LiNbO}_3]. \quad (14)$$

### 2. Case B: $\text{Nb}_2\text{O}_5$ reference state (line BC)

In this case, the Nb in  $\text{LiNbO}_3$  and  $\text{Nb}_2\text{O}_5$  are in equilibrium:

$$\mu_{\text{Nb}}^{\text{Nb}_2\text{O}_5}[\text{LiNbO}_3] = \frac{1}{2}(E_{\text{tot}}[\text{Nb}_2\text{O}_5] - 5\mu_{\text{O}}). \quad (15)$$

The chemical potential of Li in  $\text{LiNbO}_3$  can then be determined as

$$\mu_{\text{Li}}^{\text{Nb}_2\text{O}_5}[\text{LiNbO}_3] = E_{\text{tot}}[\text{LiNbO}_3] - 3\mu_{\text{O}} - \mu_{\text{Nb}}^{\text{Nb}_2\text{O}_5}[\text{LiNbO}_3]. \quad (16)$$

### 3. Reconciliation of the two reference states

One might think that these separate analyses would be equivalent. To explore this, we can take  $\mu_{\text{Li}}$  [ $\text{LiNbO}_3$ ] in Eqs. (14) and (16) in terms of individual energy contributions. From Eq. (14) we get the chemical potential for Li in  $\text{LiNbO}_3$ , with a  $\text{Li}_2\text{O}$  reference as

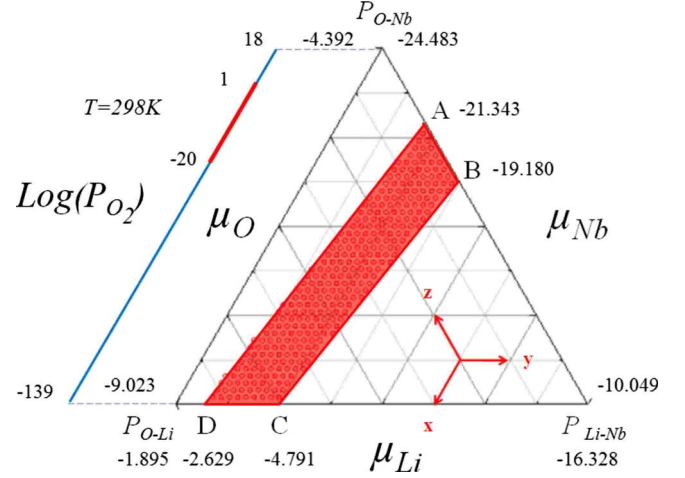


FIG. 4. (Color online) Stability range of chemical potentials (in eV) of the elements in  $\text{LiNbO}_3$ . The region enclosed by points A, D, and  $P_{\text{Li-Nb}}$  satisfies Eq. (9), while the region enclosed by points B, C,  $P_{\text{O-Li}}$ , and  $P_{\text{O-Nb}}$  satisfies Eq. (10). The intersection of these two regions defines the thermodynamically allowable range of chemical potentials. This stability region is thus defined by the shaded quadrilateral. Line AD represents using  $\text{Li}_2\text{O}$  as reference state; line BC represents using  $\text{Nb}_2\text{O}_5$  as reference. The oxygen partial pressure range (in atm) is that for room temperature.

$$\mu_{\text{Li}}^{\text{Li}_2\text{O}}[\text{LiNbO}_3] = \mu_{\text{Li}}[\text{metal}] + \frac{1}{2}\Delta H_f(\text{Li}_2\text{O}). \quad (17)$$

Likewise from Eq. (16), we can determine the chemical potential of Li in  $\text{LiNbO}_3$  with an  $\text{Nb}_2\text{O}_5$  reference as

$$\mu_{\text{Li}}^{\text{Nb}_2\text{O}_5}[\text{LiNbO}_3] = \mu_{\text{Li}}[\text{metal}] + \Delta H_f(\text{LiNbO}_3) - \frac{1}{2}\Delta H_f(\text{Nb}_2\text{O}_5). \quad (18)$$

Thus

$$\mu_{\text{Li}}^{\text{Nb}_2\text{O}_5}[\text{LiNbO}_3] - \mu_{\text{Li}}^{\text{Li}_2\text{O}}[\text{LiNbO}_3] = \Delta H_{\text{diff}}, \quad (19)$$

where

$$\Delta H_{\text{diff}} \equiv \Delta H_f(\text{LiNbO}_3) - \frac{1}{2}[\Delta H_f(\text{Nb}_2\text{O}_5) + \Delta H_f(\text{Li}_2\text{O})]. \quad (20)$$

As Table V shows, both experimental data and our GGA calculations show that  $\Delta H_{\text{diff}}$  is nonzero. As a result, the two reference states are thermodynamically different from each other.

The result of this analysis is that the chemical potentials of all three elements are constrained. The bounds that these constraints impose could be determined from experiments on the range of stability of the various oxides. Unfortunately the complete experimental data set required is not available. We therefore chose to use the results of GGA calculations to determine these constraints as we are then able to develop a completely consistent data set of chemical potentials and DFES.

TABLE III. The energies of lithium metal, niobium metal, oxygen gas, Li<sub>2</sub>O, Nb<sub>2</sub>O<sub>5</sub>, and LiNbO<sub>3</sub> as calculated by GGA.

	Space group	Energy (eV) per atom
Li (metal)	$\bar{I}m\bar{3}m$	-1.895
Nb (metal)	$\bar{I}m\bar{3}m$	-10.049
O <sub>2</sub> (gas)		-4.392
		Energy (eV) per formula unit
LiNbO <sub>3</sub>	$R\bar{3}c$	-39.552
Li <sub>2</sub> O	$Fm\bar{3}m$	-14.461
R-Nb <sub>2</sub> O <sub>5</sub>	$C2/m$	-60.319

### C. Calculation of chemical potentials: Application to LiNbO<sub>3</sub>

Using the method outlined above, the GGA calculations allow us to explicitly define the domain of possible chemical potentials. To accurately calculate the ranges of chemical potential for each element, the energies of lithium metal, niobium metal, oxygen gas, Li<sub>2</sub>O, Nb<sub>2</sub>O<sub>5</sub>, and LiNbO<sub>3</sub> have been determined using GGA (Table III). Both lithium metal and niobium metal have  $\bar{I}m\bar{3}m$  structure, whereas the molecular oxygen gas is simulated by putting an oxygen dimer in a vacuum box. Li<sub>2</sub>O has an antifluorite structure (space group:  $Fm\bar{3}m$ ), with a lattice constant of 4.57 Å.<sup>51</sup> For Nb<sub>2</sub>O<sub>5</sub>, several different structures have been reported, including R-Nb<sub>2</sub>O<sub>5</sub> ( $C2/m$ ), P-Nb<sub>2</sub>O<sub>5</sub> ( $I4_122$ ), M-Nb<sub>2</sub>O<sub>5</sub> ( $I4/mmm$ ), N-Nb<sub>2</sub>O<sub>5</sub> ( $C2/m$ ), H-Nb<sub>2</sub>O<sub>5</sub> ( $P2_1/m$ ), T-Nb<sub>2</sub>O<sub>5</sub> ( $Pbam$ ), and B-Nb<sub>2</sub>O<sub>5</sub> ( $C2/c$ ).<sup>52</sup> Among these, T-Nb<sub>2</sub>O<sub>5</sub> and B-Nb<sub>2</sub>O<sub>5</sub> are known to be high-pressure phases,<sup>53</sup> H-Nb<sub>2</sub>O<sub>5</sub> is observed to be stable at high temperatures ( $T > 1100^\circ\text{C}$ ) R-Nb<sub>2</sub>O<sub>5</sub> is metastable and transforms to P-Nb<sub>2</sub>O<sub>5</sub> on slow heating and to N-Nb<sub>2</sub>O<sub>5</sub> on rapid heating.<sup>52</sup> According to Holtzberg *et al.*,<sup>54</sup> the room-temperature phase of Nb<sub>2</sub>O<sub>5</sub> is amorphous. Here, metastable R-Nb<sub>2</sub>O<sub>5</sub> is used to determine the chemical-potential range since it is the only phase for which complete structural information is available from the literature.<sup>52</sup> As this structure probably does not correspond to the actual structure of the room-temperature phase, there will most likely be an error associated with the chemical stability range for Nb<sub>2</sub>O<sub>5</sub>, the magnitude of which we cannot assess. This error will lead to a parallel shift of line BC mentioned in Fig. 4, which will either increase or decrease the predicted chemical stability range.

The coordination numbers of the ions in the three systems can be determined from examination of the crystal structures. As shown in Table IV, both of the structurally distinct Nb ions in LiNbO<sub>3</sub> structure are sixfold coordinated. Likewise, the two structurally distinct Nb ions in R-Nb<sub>2</sub>O<sub>5</sub> are also sixfold coordinated. Moreover, the bond lengths in the two systems determined from the DFT calculations are both close to each other and to the experimental values. The situation is different for Li<sub>2</sub>O. In particular, the Li in antifluorite structured Li<sub>2</sub>O is fourfold coordinated, whereas it is sixfold coordinated in LiNbO<sub>3</sub>. Consistent with these differences in coordination, the calculated bond lengths are quite different.

The heats of formation for Li<sub>2</sub>O, Nb<sub>2</sub>O<sub>5</sub>, and LiNbO<sub>3</sub> have been calculated from the difference between energies of the oxides and composition-weighted sum of the energies of

TABLE IV. The comparison of bond lengths and coordination numbers between Li<sub>2</sub>O, Nb<sub>2</sub>O<sub>5</sub>, and LiNbO<sub>3</sub>.

		Bond length (Å)		Coordination No.
		DFT	Expt.	
LiNbO <sub>3</sub>	Li-O (S)	2.02	2.05 <sup>a</sup>	6
	Li-O (L)	2.25	2.27 <sup>a</sup>	6
	Nb-O (S)	1.90	1.88 <sup>a</sup>	6
	Nb-O (L)	2.14	2.13 <sup>a</sup>	6
Li <sub>2</sub> O	Li-O	1.98	1.98 <sup>b</sup>	4
Nb <sub>2</sub> O <sub>5</sub>	Nb-O (S)	1.95	2.02 <sup>c</sup>	6
	Nb-O (L)	2.15	2.19 <sup>c</sup>	6

<sup>a</sup>Reference 61.

<sup>b</sup>Reference 51.

<sup>c</sup>Reference 52.

the elements. From the data shown in Table V, the error associated with experimental results for Nb<sub>2</sub>O<sub>5</sub> is significantly larger than for Li<sub>2</sub>O and LiNbO<sub>3</sub>. In particular, the calculated  $\Delta H_f$  values for Li<sub>2</sub>O and LiNbO<sub>3</sub> are within 2.3% of the experimental values (Table V), whereas for Nb<sub>2</sub>O<sub>5</sub> the error is between 4% and 10% of the experimental values. This larger deviation in  $\Delta H_f$  for Nb<sub>2</sub>O<sub>5</sub> is not surprising due to the experimental uncertainties in the structure discussed above.

Using the values shown in Table III and Eqs. (2)–(10), the ranges of possible chemical potential of each element are calculated. We then consider the chemical potential of oxygen. The dependence of  $\mu_{\text{O}}$  on temperature and partial pressure can be calculated if the dependence of  $\mu_{\text{O}}[T, P^\circ]$  at one particular pressure  $P^\circ$  is known:<sup>47</sup>

$$\mu_{\text{O}}[T, P] = \mu_{\text{O}}[T, P^\circ] + \frac{1}{2}kT \ln\left(\frac{P}{P^\circ}\right). \quad (21)$$

TABLE V. The heats of formation of Li<sub>2</sub>O, Nb<sub>2</sub>O<sub>5</sub>, and LiNbO<sub>3</sub> calculated from the GGA calculations, compared with experimental results. Both experimental and calculated values are at  $T=0$  K.

	GGA (eV)	Expt. (eV)
$\Delta H(\text{Li}_2\text{O})$	-6.280	-6.139 <sup>a,b</sup>
$\Delta H(\text{Nb}_2\text{O}_5)$	-18.262	-19.202 <sup>a</sup>
		-19.943 <sup>a</sup>
		-19.687 <sup>a</sup>
		-19.722 <sup>a</sup>
		-19.887 <sup>a</sup>
		-19.735 <sup>a</sup>
		-19.666 <sup>a</sup>
		-19.813 <sup>a</sup>
		-19.687 <sup>b</sup>
$\Delta H(\text{LiNbO}_3)$	-14.433	-14.149 <sup>c</sup>
$\Delta H_{\text{diff}}$	-2.162	-1.236

<sup>a</sup>Reference 55.

<sup>b</sup>Reference 63.

<sup>c</sup>Reference 64.

TABLE VI. Change in oxygen chemical potential with respect to 0 K value from experiment (Ref. 55).

Temperature (K)	Change in $\mu_{\text{O}}$ (eV)
0	0.000
100	-0.150
200	-0.341
298.15	-0.544
300	-0.548
400	-0.765
500	-0.991
600	-1.233
700	-1.460
800	-1.702
900	-1.949
1000	-2.199

High values of  $\mu_{\text{O}}$  correspond to high oxygen partial pressures and conditions that tend to favor oxidation. Similarly, low values of  $\mu_{\text{O}}$  correspond to low partial pressures of oxygen and conditions that favor reduction. The value of  $\mu_{\text{O}}$  calculated by DFT is at 0 K. Its dependence on temperature can be derived from experimental thermodynamic data, yielding

$$\mu_{\text{O}}[T, P] = \mu_{\text{O}}[0 \text{ K}, P^{\circ}] + \frac{1}{2} \Delta G(\Delta T, P^{\circ}, \text{O}_2). \quad (22)$$

The experimentally determined temperature dependence of the oxygen chemical potential at 1 atm is given in Table VI.<sup>55</sup> The requirements of stability of  $\text{LiNbO}_3$  discussed above place limits on the oxygen partial pressures which, at 298 K, can lie in the range of  $4.9 \times 10^{-139} - 2.6 \times 10^{18}$  atm. Of course, both of these limits are physically unreasonable. Thus in Fig. 4, the more physically reasonable pressure range of  $10^{-20} - 10$  atm is also indicated.

Referring to the ternary stability map in Fig. 4, at any point within the triangle, the sum of the chemical potentials of each element yields the total energy of  $\text{LiNbO}_3$ . Furthermore, considering the constraints imposed by Eqs. (9) and (10), we can further narrow down the range of chemical potentials. The region enclosed by points A, D, and  $P_{\text{Li-Nb}}$  satisfies Eq. (9), while the region enclosed by points B, C,  $P_{\text{O-Li}}$ , and  $P_{\text{O-Nb}}$  satisfies Eq. (10). The intersection of these two regions defines the thermodynamically allowable range of chemical potentials. This stability region is thus defined by the shaded quadrilateral enclosed by points A–D. Therefore, to study the general case, the DFE calculations for all points within the stability range are performed. At this point, all of the methods needed for defect-energy calculations are defined. In Sec. IV, we present the results.

#### IV. DFEs IN $\text{LiNbO}_3$

The current paper focuses on the following intrinsic defects: Li-Frenkel, Nb-Frenkel, O-anti-Frenkel,  $\text{Li}_2\text{O}$ -pseudo-

Schottky,  $\text{Nb}_2\text{O}_5$ -pseudo-Schottky,  $\text{LiNbO}_3$ -Schottky, and three defect clusters that have been discussed in the literature:  $5\text{Nb}_{\text{Li}}^{\cdots\cdots} + 4\text{V}_{\text{Nb}}^{\prime\prime\prime\prime}$ ,  $2\text{Nb}_{\text{Li}}^{\cdots\cdots} + 3\text{V}_{\text{Li}}^{\prime} + \text{V}_{\text{Nb}}^{\prime\prime\prime\prime}$ , and  $\text{Nb}_{\text{Li}}^{\cdots\cdots} + 4\text{V}_{\text{Li}}^{\prime}$ .<sup>4</sup>

For computational efficiency, the DFEs of these intrinsic-defect complexes are first determined from the formation energies of the individual charged defects that make up the complex. Thus, the formation energy of  $\text{Li}_2\text{O}$ -pseudo-Schottky comes from separate calculations on the formation energy of lithium vacancy and oxygen vacancy. The association energy resulting from the interaction of the individual charged defects in these neutral defect clusters will be discussed in Sec. IV D.

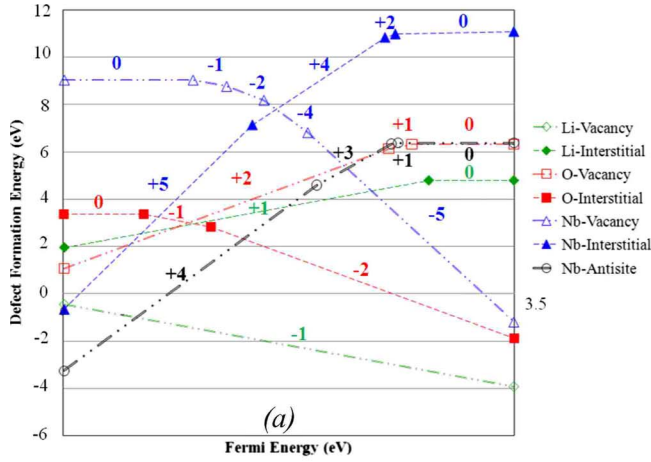
Before characterizing the defect clusters, it is important to analyze the individual defects with various charge states. Section IV A will discuss all the results obtained for individual defects followed by the neutral charged clusters.

#### A. DFEs of single-point defects

The DFEs of all the native point defects with various charge states in  $\text{LiNbO}_3$  have been calculated using Eq. (1). The interstitial sites are assumed to be at (0.0,0.0,0.139 36) for individual defects, which corresponds to the center of an empty oxygen octahedron. Since the DFE depends on the location of the Fermi energy, the influence of the Fermi energy on the stability of each individual defect is considered. In the current study, the reference zero of Fermi energy is assigned to be the VBM of the perfect structure. The highest Fermi energy thus corresponds to the conduction-band minimum (CBM). As discussed by Van de Walle *et al.*,<sup>22</sup> it is necessary to implement an additional procedure to calculate the shift of bands caused by the presence of defects. Thus, to calculate this shift, the average electrostatic potential difference [ $\Delta V$  in Eq. (1)] between the perfect structure and the defected structure has been determined using the approach of Kohan *et al.*<sup>23</sup>

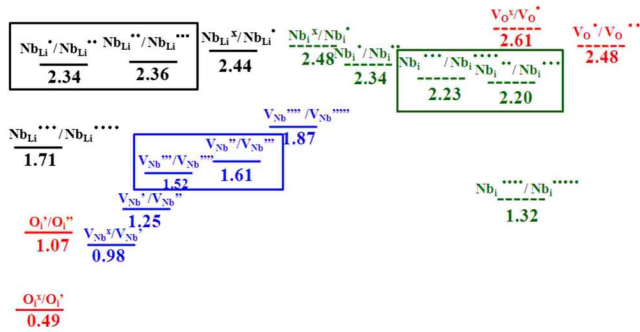
For pure stoichiometric  $\text{LiNbO}_3$ , which is an insulator, the Fermi energy is expected to be at the middle of the band gap. In the present paper, we are simulating the dilute limit of pure stoichiometric system; therefore the shift of Fermi energy is considered negligible. The dependence of DFEs on the Fermi level is shown in Fig. 5(a), using  $\text{Nb}_2\text{O}_5$  (the BC line in Fig. 4) as the reference state. For each individual defect, Fig. 5 includes only the charge states with lowest DFE values over the corresponding Fermi-level range. The slopes of the lines in the Fig. 5(a) represent the charge states of the defects. When the Fermi energy is at the middle of the band gap,  $\text{V}_{\text{Li}}^{\prime}$ ,  $\text{V}_{\text{Nb}}^{\prime\prime\prime\prime}$ ,  $\text{V}_{\text{O}}^{\cdot\cdot}$ ,  $\text{Nb}_{\text{Li}}^{\cdots\cdots}$ ,  $\text{Li}_i^{\cdot}$ ,  $\text{Nb}_i^{\cdots\cdots}$ , and  $\text{O}_i^{\cdot\cdot}$  are the energetically favored charge state for each defect. It is also observed that as the Fermi energy increases (i.e., moves from the VBM toward the CBM), the thermodynamically stable charge of the positive defects decreases. Correspondingly, the charge states of the negative defects decrease as the Fermi energy increases. This order of stability is broadly consistent with that determined in the DFT calculations of Li *et al.*<sup>27</sup>

In Fig. 5(a), the points at which the slopes change are the thermodynamic transition levels,  $\varepsilon(q_1/q_2)$ . At these transi-



3.5

CBM



0.0

(b)

VBM

FIG. 5. (Color online) (a) Defect formation energies of various point defects as a function of Fermi energy; the lowest-energy charge state is given in each case. The Fermi energy ranges from  $E_F=0$  (left) at the VBM to  $E_F=3.5$  eV at the conduction-band minimum (right). (b) Thermodynamic transition levels of O-related and Nb-related defects. The values under the line are with respect to the VBM. The transitions enclosed by squares have a negative  $U$  character.

tion points the Fermi levels of the charge states  $q_1$  and  $q_2$  have the same energy. For Nb-related defects, the stable Nb antisite changes from 3+ to 1+ directly without passing through the 2+ charge state. Correspondingly, the Nb interstitial changes from 2+ to 0, and the Nb vacancy changes from 2- to 4-. To characterize this phenomenon, the thermodynamic transition level of adjacent charge states of Nb-related and O-related defects are calculated and shown in Fig. 5(b). It can be seen that there are order switchings for the Nb antisite, Nb interstitial, and Nb vacancy. The Nb antisite  $\epsilon(1+/2+)$  is lower than the Nb antisite  $\epsilon(2+/3+)$ . For the Nb interstitial,  $\epsilon(2+/3+)$  is lower than  $\epsilon(3+/4+)$ . For the Nb vacancy,  $\epsilon(3-/4-)$  is lower than the Nb vacancy  $\epsilon(2-/3-)$ . These switchings of the order of thermodynamic transition levels are indicative of the so-called negative  $U$  effects.<sup>56</sup> However, as Fig. 5(b) shows, the energies for the thermodynamic transition levels for the respective Nb-related defects discussed above are extremely close to each other. Indeed they are close to the estimated uncertainties in the present calculations.

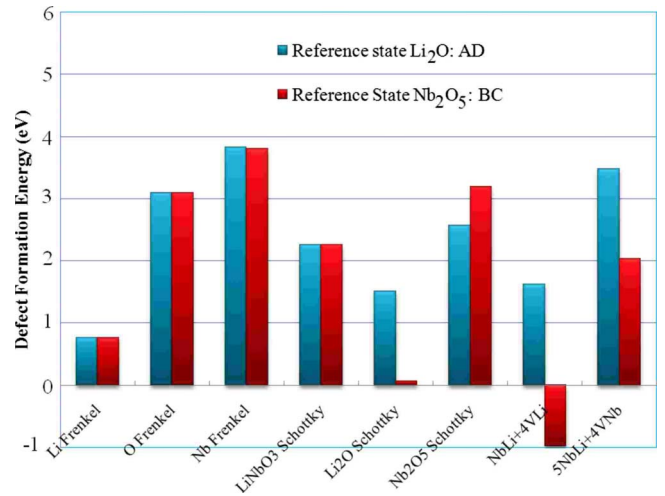


FIG. 6. (Color online) Formation energies of neutral defects and defect clusters under  $\text{Nb}_2\text{O}_5$ -rich conditions (right=red) and  $\text{Li}_2\text{O}$ -rich conditions (left=blue).

The electron-lattice interaction results in different atomic relaxations for different charge states of the defects. Taking the Nb antisite as an example, the average bond length of 0, 1+, 2+, 3+, and 4+ are 2.130, 2.092, 2.063, 2.038, and 2.011 Å, respectively. These decreases in bond lengths as the charge state of Nb antisite increases are due to the increasing electrostatic interactions.

**B. Formation energies of charge-neutral defect complexes**

The constraint of charge neutrality means that only neutral defect complexes will be present in the system. While this leads to a need to consider a plethora of different defect clusters, it does provide the simplification of not having to consider the effects of the Fermi energy since this term drops out in Eq. (1). In the current section, the charged defects that make the neutral defect are assumed to be infinitely far away from each other. The association effects are added in Sec. III D.

From Fig. 6, it is can be seen that formation energies of the  $\text{Li}$ -Frenkel,  $\text{O}$ -anti-Frenkel,  $\text{Nb}$ -Frenkel, and  $\text{LiNbO}_3$ -Schottky are independent of the choice of the chemical potential. This is because these defects preserve the stoichiometry of the system, obviating any chemical-potential term. By contrast, the  $\text{Li}_2\text{O}$ -pseudo-Schottky,  $\text{Nb}_2\text{O}_5$ -pseudo-Schottky,  $5\text{Nb}_{\text{Li}} + 4\text{V}_{\text{Nb}}$ ,  $2\text{Nb}_{\text{Li}} + 3\text{V}_{\text{Li}} + \text{V}_{\text{Nb}}$ , and  $\text{Nb}_{\text{Li}} + 4\text{V}_{\text{Li}}$  defect clusters change the stoichiometry of the system. Thus their formation energies are influenced by the reference state of chemical potential. The calculations show that the formation energies for Nb antisite compensated purely by Nb vacancies ( $5\text{Nb}_{\text{Li}} + 4\text{V}_{\text{Nb}}$ ) is different for the two reference states. However it is energetically unfavorable under both conditions. The DFE for  $\text{Nb}_{\text{Li}} + 4\text{V}_{\text{Li}}$  clusters is positive with the  $\text{Li}_2\text{O}$  (AD in Fig. 4) reference state but negative for the  $\text{Nb}_2\text{O}_5$  (BC in Fig. 4) reference state, indicating that this defect cluster will occur spontaneously under  $\text{Nb}_2\text{O}_5$ -rich conditions.

The Frenkel defects analyzed above consist of individual fully charged defects. Frenkel defects with partial charged or

TABLE VII. Defect formation energies for various defects, compared with previous electronic-structure and atomistic simulations.

Defects (eV/defect)	Araujo (atomistic) <sup>a</sup>	Donnerberg (atomistic) <sup>b</sup>	USPP-LDA <sup>c</sup>	PAW-GGA	PAW-GGA
Reference state	None	None	Nb <sub>2</sub> O <sub>5</sub>	Nb <sub>2</sub> O <sub>5</sub>	Li <sub>2</sub> O
Li-Frenkel	1.37	0.93	1.78	0.77	0.77
Nb-Frenkel	11.72	6.26	6.43	3.80	3.80
O-Frenkel	4.76	3.42	5.80	3.10	3.10
LiNbO <sub>3</sub> -Schottky	3.95	3.91	4.84	2.25	2.25
Li <sub>2</sub> O-pseudo-Schottky	1.81	1.94	-0.89	0.07	1.51
Nb <sub>2</sub> O <sub>5</sub> -pseudo-Schottky	5.09	2.85	7.29	3.19	2.57
Nb <sub>Li</sub> <sup>••••</sup> +4V <sub>Li</sub> <sup>'</sup>	1.51	2.74	-4.40	-0.98	1.62
5Nb <sub>Li</sub> <sup>••••</sup> +4V <sub>Nb</sub> <sup>''''</sup>	10.23	5.06	2.08	2.03	3.47

<sup>a</sup>Reference 65.  
<sup>b</sup>Reference 26.  
<sup>c</sup>Reference 27.

neutral individual defects can also be considered. However, the formation energies of Frenkel defects with partial charged or neutral individual defects all turn out to have higher energies than those formed from fully charged individual defects. For example, the formation energy of the Frenkel defects consisting of Li<sub>i</sub><sup>x</sup>+V<sub>Li</sub><sup>x</sup> is 1.9 eV higher than the Frenkel defect formed from Li<sub>i</sub>+V<sub>Li</sub><sup>'</sup>.

Table VII compares the results of our DFT calculations with the previous DFT calculations and with calculations using empirical potentials. For the purposes of comparison, it is instructive to distinguish between those neutral defects that maintain the system stoichiometry (Li-Frenkel, Nb-Frenkel, O-Frenkel, and LiNbO<sub>3</sub>-Schottky) and those defects and defect clusters that do not maintain the system stoichiometry. For the stoichiometric defects, all four calculations conclude that the Li-Frenkel defect has the lowest formation energy. They also all predict that the Nb-Frenkel has the highest DFE. Three of the four calculations conclude that the LiNbO<sub>3</sub>-Schottky has a lower DFE than the O-Frenkel, with only the older atomistic calculations of Donnerberg *et al.*<sup>15</sup> giving the opposite order.

Turning to the nonstoichiometric defects, it is difficult to compare the results from the atomistic simulations with the DFT calculations since the atomistic calculations neither include an explicit reference nor take into account the chemical potential. However, the results of the DFT calculations<sup>27</sup> can be compared, despite the concerns with the previous DFT calculations mentioned in Sec. I. In particular the USPP and PAW calculations yield the same order of stability of defects for the Nb<sub>2</sub>O<sub>5</sub> reference state, with the Nb<sub>Li</sub><sup>••••</sup>+4V<sub>Li</sub><sup>'</sup> cluster having the lowest energy which, importantly, both analyses predict to be negative. This is strong evidence that this defect cluster should form spontaneously in Nb<sub>2</sub>O<sub>5</sub>-rich environments. Although they agree in the order of stability of the defects, the corresponding USPP and PAW calculations yield considerably different specific values for DFEs. Unfortunately the paper of Li *et al.*<sup>27</sup> does not break down the final DFEs into the contributions from the presence of the defect and the contributions from the chemical potentials. It is thus

not possible to analyze these differences further.

C. Defect stability range

The DFEs calculated so far using DFT are based on specific chemical potentials. Knowledge of the defect formation dependence over the whole chemical potential stability range is also of considerable importance. The lowest-energy defect as a function of chemical potential of each element is given in Fig. 7. It is observed that Li-Frenkel and Nb<sub>Li</sub><sup>••••</sup>+4V<sub>Li</sub><sup>'</sup> are the two important defects. The Li-Frenkel is the dominant defect within region AEFD (in Fig. 4), whereas the Nb<sub>Li</sub><sup>••~••</sup>+4V<sub>Li</sub><sup>'</sup> cluster is the dominant defect within region EBCF (in Fig. 4).

As discussed above, the dominant defects might change as μ<sub>O</sub> from its maximum (oxidizing conditions) to its minimum (reducing conditions). Remarkably, however, the Li-Frenkel is the dominant defect throughout the whole range of

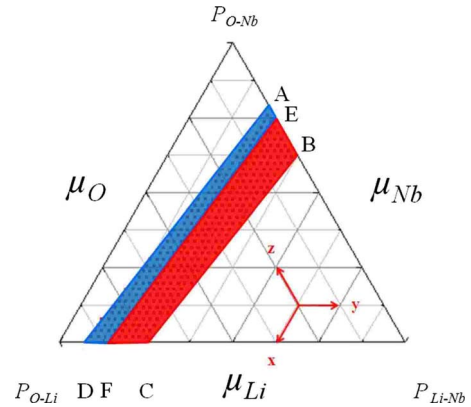


FIG. 7. (Color online) Defect stability range: in region AEFD, the Li-Frenkel is the dominant defect reaction, whereas in EBCF, the niobium antisite compensated by lithium vacancies is dominant. The Li-Frenkel is the dominant defect throughout the whole range of μ<sub>O</sub> along line AD, while the Nb<sub>Li</sub><sup>••~••</sup>+4V<sub>Li</sub><sup>'</sup> cluster dominates along BC for all oxygen partial pressures.

TABLE VIII. Association energy of  $\text{Li}_2\text{O}$ -pseudo-Schottky,  $\text{Nb}_2\text{O}_5$ -pseudo-Schottky,  $5\text{Nb}_{\text{Li}}^{\cdot\cdot\cdot\cdot} + 4\text{V}_{\text{Nb}}^{\text{''''}}$ , and  $\text{Nb}_{\text{Li}}^{\cdot\cdot\cdot\cdot} + 4\text{V}_{\text{Li}}^{\prime}$ .

	Association energy
$\text{Li}_2\text{O}$ Schottky	-0.23
$\text{Nb}_2\text{O}_5$ Schottky	-1.20
$\text{Nb}_{\text{Li}}^{\cdot\cdot\cdot\cdot} + 4\text{V}_{\text{Li}}^{\prime}$	-0.25
$5\text{Nb}_{\text{Li}}^{\cdot\cdot\cdot\cdot} + 4\text{V}_{\text{Nb}}^{\text{''''}}$	-1.12

$\mu_{\text{O}}$  along the AD line, while the  $\text{Nb}_{\text{Li}}^{\cdot\cdot\cdot\cdot} + 4\text{V}_{\text{Li}}^{\prime}$  cluster dominates along BC for all oxygen partial pressures.

#### D. Association effects

The above defect reaction analysis is based on the formation energies of individual point defect. That is, the defects are assumed to be so far away from each other that there is no interaction between them. Here, the validity of this approximation is examined by calculating the formation energies of the clustered defects. The change in energy relative to the well-separated defects is the association energy: negative association energy corresponds to the preference for the defects to cluster. Calculations of such associated clusters require the choice of specific defect arrangements. For the Frenkel defects, the vacancy and interstitial are assumed to be first neighbors. For the  $\text{Li}_2\text{O}$ -pseudo-Schottky, an oxygen atom and two lithium atoms in its first-nearest neighbor have been removed from the system. For the  $\text{Nb}_2\text{O}_5$ -pseudo-Schottky, two nearest Nb atoms are removed along with five oxygen atoms which are the first-nearest neighbor positions to the removed Nb atoms. The arrangement for the  $\text{Nb}_{\text{Li}}^{\cdot\cdot\cdot\cdot} + 4\text{V}_{\text{Li}}^{\prime}$  follows the model of Kim *et al.*,<sup>57</sup> which assumes that the defect complexes are composed of a niobium antisite surrounded by three Li vacancies in the nearest neighbor positions plus one independent vacancy

along the  $z$  direction. We analyze different possible arrangements for these defects elsewhere.<sup>58</sup> For  $5\text{Nb}_{\text{Li}}^{\cdot\cdot\cdot\cdot} + 4\text{V}_{\text{Nb}}^{\text{''''}}$  initially a Li site is chosen and replaced with an Nb atom. Then four of the first-nearest Li atom sites are replaced with Nb to obtain the  $5\text{Nb}_{\text{Li}}^{\cdot\cdot\cdot\cdot}$  configuration. Four Nb sites which are the nearest neighbors of the first Li atom replaced are then removed from the system to create  $4\text{V}_{\text{Nb}}^{\text{''''}}$ .

In all cases shown in Table VIII, the defects have a tendency to cluster, as evidenced by negative association energies. Since this association does not change any of the thermodynamics of the system, these differences in energy are independent of the reference state. Interestingly, although association lowers the energy of all of the defect clusters analyzed, it does not change their relative order. This gives us high confidence that the conclusions drawn from the isolated defect calculations are valid. The simulations of Li, Nb, and O Frenkel pairs resulted in the perfect structure with no defects since the vacancies and interstitials of the corresponding pairs were too close to each other.

#### V. DISCUSSION AND CONCLUSIONS

As discussed in Sec. I, the x-ray and NMR measurements do not provide a consistent picture of the defects in  $\text{LiNbO}_3$ . The x-ray data indicate that the oxygen vacancy concentration is negligible, i.e., that there are no model I defects ( $\text{V}_{\text{O}}^{\cdot\cdot} + 2\text{V}_{\text{Li}}^{\prime}$ ). In contrast, NMR suggests that there are almost equal numbers of model I and model III defects ( $\text{Nb}_{\text{Li}}^{\cdot\cdot\cdot\cdot} + 4\text{V}_{\text{Li}}^{\prime}$ ). It is of considerable interest to analyze our results to see if they can shed any light on this issue.

With reference to the thermodynamic analysis, it is clear that room temperature and standard pressure ( $\mu_{\text{O}}[\text{LiNbO}_3] = \mu_{\text{O}}[\text{gas}]$ ) are most relevant for applications. Thus the following analysis is performed under these conditions. However, the DFE still cannot be uniquely determined since the separate values of the chemical potentials of lithium and niobium cannot be determined uniquely, but are coupled.

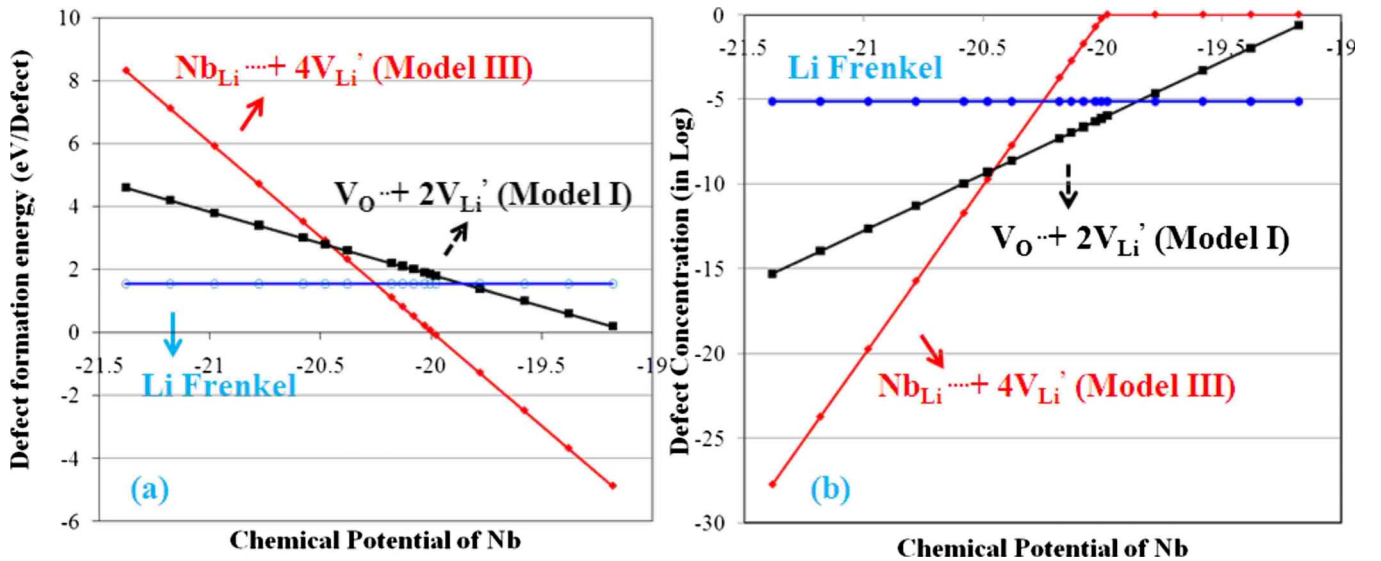


FIG. 8. (Color online) (a) The DFEs of  $\text{Nb}_{\text{Li}}^{\cdot\cdot\cdot\cdot} + 4\text{V}_{\text{Li}}^{\prime}$ , Li-Frenkel, and  $\text{V}_{\text{O}}^{\cdot\cdot} + 2\text{V}_{\text{Li}}^{\prime}$  as a function of niobium chemical potential. (b) The defect concentration caused by  $\text{Nb}_{\text{Li}}^{\cdot\cdot\cdot\cdot} + 4\text{V}_{\text{Li}}^{\prime}$ , Li-Frenkel and  $\text{V}_{\text{O}}^{\cdot\cdot} + 2\text{V}_{\text{Li}}^{\prime}$  as a function of niobium chemical potential.

Our calculations are consistent with the experiments in that they indicate that both model I and model III are energetically favorable relative to most other defect structures. In particular, as shown in Fig. 8(a), model III and the Li-Frenkel are the dominant defects under different conditions, while model I has the second lowest DFE through most of the chemical potential stability range. The error of 0.2 eV represent our estimated uncertainty in the formation energies. The Li-Frenkel defects do not, of course, change the stoichiometry of the system and are thus not relevant with regards to interpreting the x-ray and NMR data.

The concentrations of each defect can be calculated from

$$C_d = N_{\text{site}} \exp(-\Delta G_f/kT), \quad (23)$$

where  $C_d$  is the number of the defects,  $N_{\text{site}}$  is the number of sites in the crystal where the defect could occur,  $k$  is the Boltzmann constant, and  $T$  is the temperature. The calculated defect concentrations are shown in Fig. 8(b). This figure must be interpreted with caution since negative formation energy would apparently lead to a concentration of unity for the corresponding defect, which is not reasonable since the calculations on which Fig. 8(b) is based assume a dilute solution of defects. Presumably the formation energies will increase with increasing concentration, such that the system remains stable. For low Nb chemical potentials (Li-rich conditions), the Li-Frenkel is the dominant defect, with a small admixture of model I. At higher Nb chemical potentials, model III is dominant and produces a concentration of lithium vacancies that is at least 2 orders of magnitude larger than that produced by model I. Since model I defects lead to oxygen vacancies while model III defects do not, this would be consistent with the experimental finding<sup>14</sup> that for Nb-rich conditions, oxygen vacancies concentration is much smaller than the lithium vacancy concentrations. However, it should be noted that although the defect concentration of model I is much smaller than that of model III, it may still reach substantial levels under these Nb-rich conditions. In order to achieve the experimentally postulated ratio of 1.1:1 for model I and model III, the DFEs of these two defect reactions would have to be much more similar in magnitude than they are calculated to be. Thus this study does not support this scenario.

We finally address the mechanism for the vapor-transport equilibration (VTE) method<sup>3</sup> used widely in transforming a congruent composition of lithium niobate into a stoichiometric composition. In the VTE method,<sup>59</sup> a target wafer is exposed to  $\text{Li}_2\text{O}$  vapor produced by decomposition of  $\text{Li}_2\text{CO}_3$  at high temperature ( $>730$  °C).<sup>60</sup> This produces a

constant vapor pressure of  $\text{Li}_2\text{O}$  equal to the vapor pressure of stoichiometric  $\text{LiNbO}_3$ . The wafer, which is congruent  $\text{LiNbO}_3$  and deficient in  $\text{Li}_2\text{O}$ , absorbs  $\text{Li}_2\text{O}$  from the vapor until it reaches the stoichiometric composition. Then Li diffuses into a considerable depth due to the high diffusivity. The whole growth procedure is thus under  $\text{Li}_2\text{O}$ -rich conditions. In the language of our calculations, this experimental VTE procedure thus corresponds to using  $\text{Li}_2\text{O}$  as the reference state. Therefore, according to the analysis in Sec. IV C, the lithium Frenkel defect is predicted to be the most stable, with a positive DFE. Using Eq. (23), the concentration of defect is predicted to be negligible, which results in a stoichiometric composition.

Our calculations thus indicate that the relative energetics of the defect clusters can change under variation in temperatures and chemical potentials during annealing experiments, which may result in different relative abundances.<sup>25</sup> Furthermore, these results strongly suggest that the defect chemistry can be expected to be sensitive to the thermal and chemical history of the sample, making direct comparisons among experimental results difficult. Indeed, this sensitivity could be the origin of some of the experimental inconsistencies.

In summary, the intrinsic defects and defect clusters in  $\text{LiNbO}_3$  have been characterized using DFT-PAW approach. The formation energies of various types of defects and defect clusters have been reported and the dominant defects are determined over the chemical potential stability range. The association effects have also been investigated. The Li-Frenkel was found to have the lowest DFE under  $\text{Li}_2\text{O}$ -rich conditions, while the cluster consisting of a niobium antisite compensated by lithium vacancy ( $\text{Nb}_{\text{Li}}^{\cdots} + 4V_{\text{Li}}^{\prime}$ ) was found to be energetically stable under  $\text{Nb}_2\text{O}_5$ -rich conditions.

These results are consistent with experimental observations. In particular, the intrinsic defect cluster mentioned above, which was conjectured before to play a critical role in domain structure and dynamics, has been verified using first-principles calculations to indeed have the lowest formation energy. The defect analysis also sheds light on the mechanism by which a congruent composition of  $\text{LiNbO}_3$  can be transformed into a stoichiometric composition by the widely used VTE method today.

#### ACKNOWLEDGMENTS

This work was supported by the National Science Foundation under Grants No. DMR-0602986 and No. DMR-0303279. The authors also thank the High Performance Center (HPC) at University of Florida for providing resources to perform the DFT calculations.

\*Present address: Materials Science Division, Argonne National Laboratory, Argonne, IL 60439.

†Corresponding author; sphil@mse.ufl.edu

<sup>1</sup>K. K. Wong, *Properties of Lithium Niobate* (INSPEC, Stevenage, Herts, UK, 2002).

<sup>2</sup>G. D. Boyd, K. Nassau, R. C. Miller, W. L. Bond, and A. Sav-

age, *Appl. Phys. Lett.* **5**, 234 (1964).

<sup>3</sup>F. S. Chen, *J. Appl. Phys.* **40**, 3389 (1969).

<sup>4</sup>V. Gopalan, V. Dierolf, and D. A. Scrymgeour, *Annu. Rev. Mater. Res.* **37**, 449 (2007).

<sup>5</sup>L. Tian, V. Gopalan, and L. Galambos, *Appl. Phys. Lett.* **85**, 4445 (2004).

- <sup>6</sup>P. F. Bordui, R. G. Norwood, D. H. Jundt, and M. M. Fejer, *J. Appl. Phys.* **71**, 875 (1992).
- <sup>7</sup>K. Kitamura, J. K. Yamamoto, N. Iyi, S. Kimura, and T. Hayashi, *J. Cryst. Growth* **116**, 327 (1992).
- <sup>8</sup>K. Kitamura, Y. Furukawa, K. Niwa, V. Gopalan, and T. E. Mitchell, *Appl. Phys. Lett.* **73**, 3073 (1998).
- <sup>9</sup>V. Gopalan and M. C. Gupta, *Appl. Phys. Lett.* **68**, 888 (1996).
- <sup>10</sup>V. Gopalan, T. E. Mitchell, Y. Furukawa, and K. Kitamura, *Appl. Phys. Lett.* **72**, 1981 (1998).
- <sup>11</sup>C. Baumer, C. David, A. Tunyagi, K. Betzler, H. Hesse, E. Kratzig, and M. Wohlecke, *J. Appl. Phys.* **93**, 3102 (2003).
- <sup>12</sup>A. Prokhorov and I. Kuzminov, *Physics and Chemistry of Crystalline Lithium Niobate* (Hilger, Bristol, New York, 1990).
- <sup>13</sup>Y. H. Han and D. M. Smyth, *Am. Ceram. Soc. Bull.* **62**, 852 (1983).
- <sup>14</sup>O. F. Schirmer, O. Thiemann, and M. Wohlecke, *J. Phys. Chem. Solids* **52**, 185 (1991).
- <sup>15</sup>H. Donnerberg, S. M. Tomlinson, C. R. A. Catlow, and O. F. Schirmer, *Phys. Rev. B* **44**, 4877 (1991).
- <sup>16</sup>N. Iyi, K. Kitamura, F. Izumi, J. K. Yamamoto, T. Hayashi, H. Asano, and S. Kimura, *J. Solid State Chem.* **101**, 340 (1992).
- <sup>17</sup>N. Zotov, H. Boysen, F. Frey, T. Metzger, and E. Born, *J. Phys. Chem. Solids* **55**, 145 (1994).
- <sup>18</sup>G. S. Zhdanov, S. A. Ivanov, E. V. Kolontsova, and A. E. Korneev, *Ferroelectrics* **21**, 463 (1978).
- <sup>19</sup>S. A. Ivanov, A. E. Korneyev, E. V. Kolontsova, and Y. N. Venevtsev, *Kristallografiya* **23**, 1071 (1978).
- <sup>20</sup>E. M. Ivanova, N. A. Sergeev, and A. V. Yatsenko, *Crystallogr. Rep.* **43**, 303 (1998).
- <sup>21</sup>A. V. Yatsenko, E. N. Ivanova, and N. A. Sergeev, *Physica B* **240**, 254 (1997).
- <sup>22</sup>C. G. Van de Walle and J. Neugebauer, *J. Appl. Phys.* **95**, 3851 (2004).
- <sup>23</sup>A. F. Kohan, G. Ceder, D. Morgan, and Chris G. Van de Walle, *Phys. Rev. B* **61**, 15019 (2000).
- <sup>24</sup>J. He, R. K. Behera, M. W. Finnis, X. Li, E. C. Dickey, S. R. Phillpot, and S. B. Sinnott, *Acta Mater.* **55**, 4325 (2007).
- <sup>25</sup>V. Dierolf and C. Sandmann, *J. Lumin.* **125**, 67 (2007).
- <sup>26</sup>H. Donnerberg, S. M. Tomlinson, C. R. A. Catlow, and O. F. Schirmer, *Phys. Rev. B* **40**, 11909 (1989).
- <sup>27</sup>Q. K. Li, B. Wang, C. H. Woo, H. Wang, and R. Wang, *J. Phys. Chem. Solids* **68**, 1336 (2007).
- <sup>28</sup>G. Kresse and J. Furthmuller, *Comput. Mater. Sci.* **6**, 15 (1996).
- <sup>29</sup>G. Kresse and J. Furthmuller, *Phys. Rev. B* **54**, 11169 (1996).
- <sup>30</sup>P. E. Blochl, *Phys. Rev. B* **50**, 17953 (1994).
- <sup>31</sup>P. Blaha, K. Schwarz, P. Sorantin, and S. B. Trickey, *Comput. Phys. Commun.* **59**, 399 (1990).
- <sup>32</sup>D. Vanderbilt, *Phys. Rev. B* **41**, 7892 (1990).
- <sup>33</sup>P. Pulay, *Chem. Phys. Lett.* **73**, 393 (1980).
- <sup>34</sup>M. Veithen and P. Ghosez, *Phys. Rev. B* **65**, 214302 (2002).
- <sup>35</sup>K. Parlinski and Z. Q. Li, *Phys. Rev. B* **61**, 272 (2000).
- <sup>36</sup>W. Y. Ching, Z. Q. Gu, and Y. N. Xu, *Phys. Rev. B* **50**, 1992 (1994).
- <sup>37</sup>D. Redfield and W. J. Burke, *J. Appl. Phys.* **45**, 4566 (1974).
- <sup>38</sup>A. Dhar and A. Mansingh, *J. Appl. Phys.* **68**, 5804 (1990).
- <sup>39</sup>R. M. Martin, *Electronic Structure: Basic Theory and Practical Methods* (Cambridge University Press, New York, 2004).
- <sup>40</sup>H. J. Monkhorst and J. D. Pack, *Phys. Rev. B* **13**, 5188 (1976).
- <sup>41</sup>C. G. Van de Walle, P. J. H. Denteneer, Y. Bar-Yam, and S. T. Pantelides, *Phys. Rev. B* **39**, 10791 (1989).
- <sup>42</sup>S. G. Louie, M. Schluter, J. R. Chelikowsky, and M. L. Cohen, *Phys. Rev. B* **13**, 1654 (1976).
- <sup>43</sup>W. E. Pickett, K. M. Ho, and M. L. Cohen, *Phys. Rev. B* **19**, 1734 (1979).
- <sup>44</sup>G. Makov and M. C. Payne, *Phys. Rev. B* **51**, 4014 (1995).
- <sup>45</sup>U. Gerstmann, E. Rauls, T. Frauenheim, and H. Overhof, *Phys. Rev. B* **67**, 205202 (2003).
- <sup>46</sup>D. Segev and S. H. Wei, *Phys. Rev. Lett.* **91**, 126406 (2003).
- <sup>47</sup>K. Reuter and M. Scheffler, *Phys. Rev. B* **65**, 035406 (2001).
- <sup>48</sup>P. Erhart and K. Albe, *J. Appl. Phys.* **102**, 084111 (2007).
- <sup>49</sup>K. Matsunaga, T. Tanaka, T. Yamamoto, and Y. Ikuhara, *Phys. Rev. B* **68**, 085110 (2003).
- <sup>50</sup>R. DeHoff, *Thermodynamics in Materials Science* (Taylor & Francis, Boca Raton, FL, 2006).
- <sup>51</sup>T. W. D. Farley, W. Hayes, S. Hull, R. Ward, M. T. Hutchings, and M. Alba, *Solid State Ionics* **28**, 189 (1988).
- <sup>52</sup>J. B. Goodenough and A. Hamnett, *Physics of Non-tetrahedrally Bonded Binary Compounds III* (Springer-Verlag, Berlin, 1984).
- <sup>53</sup>I. P. Zibrov, V. P. Filonenko, P. E. Werner, B. O. Marinder, and M. Sundberg, *J. Solid State Chem.* **141**, 205 (1998).
- <sup>54</sup>F. Holtzberg, A. Reisman, M. Berry, and M. Berkenblit, *J. Am. Chem. Soc.* **78**, 1536 (1956).
- <sup>55</sup>J. Malcolm and W. Chase, *NIST-JANAF Thermochemical Tables* (American Chemical Society, Washington, DC, 1998).
- <sup>56</sup>P. W. Anderson, *Phys. Rev. Lett.* **34**, 953 (1975).
- <sup>57</sup>S. Kim, V. Gopalan, K. Kitamura, and Y. Furukawa, *J. Appl. Phys.* **90**, 2949 (2001).
- <sup>58</sup>H. Xu, D. Lee, J. He, S. B. Sinnott, and S. R. Phillpot (unpublished).
- <sup>59</sup>R. L. Holman, *Processing of Crystalline Ceramics* (Plenum, New York, 1978).
- <sup>60</sup>J. Zou, S. M. Zhou, J. Xu, L. H. Zhang, Z. L. Xie, P. Han, and R. Zhang, *J. Appl. Phys.* **98**, 084909 (2005).
- <sup>61</sup>S. C. Abrahams and P. Marsh, *Acta Crystallogr., Sect. B: Struct. Sci.* **42**, 61 (1986).
- <sup>62</sup>H. Boysen and F. Altorfer, *Acta Crystallogr., Sect. B: Struct. Sci.* **50**, 405 (1994).
- <sup>63</sup>I. Barin, O. Knacke, and O. Kubaschewski, *Thermochemical Properties of Inorganic Substances: Supplement* (Springer-Verlag, New York, 1977).
- <sup>64</sup>O. Knacke, O. Kubaschewski, and K. Hesselmann, *Thermochemical Properties of Inorganic Substances* (Spring, Berlin, 1991).
- <sup>65</sup>R. M. Araujo, K. Lengyel, R. A. Jackson, L. Kovacs, and M. E. G. Valerio, *J. Phys.: Condens. Matter* **19**, 046211 (2007).